

UNCLASSIFIED

Defense Technical Information Center
Compilation Part Notice

ADP011500

TITLE: Electronic Structure, Amorphous Morphology and Thermal Stability of Transition Metal Oxide and Chalcogenide Alloys

DISTRIBUTION: Approved for public release, distribution unlimited

This paper is part of the following report:

TITLE: International Workshop on Amorphous and Nanostructured Chalcogenides 1st, Fundamentals and Applications held in Bucharest, Romania, 25-28 Jun 2001. Part 1

To order the complete compilation report, use: ADA398590

The component part is provided here to allow users access to individually authored sections of proceedings, annals, symposia, etc. However, the component should be considered within the context of the overall compilation report and not as a stand-alone technical report.

The following component part numbers comprise the compilation report:
ADP011500 thru ADP011563

UNCLASSIFIED

ELECTRONIC STRUCTURE, AMORPHOUS MORPHOLOGY AND THERMAL STABILITY OF TRANSITION METAL OXIDE AND CHALCOGENIDE ALLOYS

G. Lucovsky

Departments of Physics, Electrical and Computer Engineering, and Materials Science and Engineering, North Carolina State Univ., Raleigh, NC 27695, USA

This paper is presented to honor Professor Radu Grigorovici at his 90th birthday celebration for his outstanding contributions to the chemical bonding and atomic structure of amorphous semiconductors, including the chalcogenides that are highlighted at this conference. A chemical bonding approach is applied in this paper to non-crystalline transition metal oxides and their silicate and aluminate alloys. Transition metal oxides and alloys are considerably more ionic than SiO_2 , and this increased ionicity, along with the localized electronic structure associated with transition metal atom d-states is the basis for the significant differences in their optical and electrical properties. This paper also provides new insights into the electronic structure of transition metal chalcogenide alloys.

(Received June 4, 2001; accepted June 11, 2001)

Keywords: Chalcogenide alloys, Electronic structure, Thermal stability

1. Introduction

Interest in the electronic structure of amorphous semiconductors was stimulated by two advances in technology that occurred more than 25 years ago: i) the discovery of reversible and irreversible electronic and optical switching in chalcogenide alloys by Ovshinsky and his coworkers at Energy Conversion Devices, ECD [1,2], and ii) the fabrication of photovoltaic devices in hydrogenated amorphous silicon by Carlson and Wronski at RCA [3]. These advances in technology resulted in a world-wide interest in the properties of amorphous semiconductors, including Si and Ge, the elemental and compound chalcogenides, as well as *more complex* chalcogenide alloys. Whilst the primary dedication of this paper is to Professor Radu Grigorovici for his pioneering work in chemical bonding, atomic structure, and transport and optical properties of chalcogenides and other elemental amorphous semiconductors, three other pioneers in this field warrant recognition as well. These are i) Sir Neville Mott for the role he and his coworkers at University of Cambridge and elsewhere played in the development of a microscopic understanding of the electronic properties of amorphous semiconductors [4], iii) Josef Stuke for his pioneering studies of crystalline Se and Te, and transport properties of amorphous Si and Ge [5,6], and finally, iii) Stan Ovshinsky for having the courage, determination and remarkable insight to seek, and to find new and *unanticipated* properties in complex chalcogenide alloys that were well outside of the *comfortable envelope of the prevailing conventional wisdom* [1,2].

The primary motivation for the research presented in this paper has been the search for new dielectric materials for advanced Si devices. Non-crystalline alloys of group IIIB and IVB transition metal oxides and rare earth oxides, e.g., $\text{Y}(\text{La})_2\text{O}_3$ and $\text{Zr}(\text{Hf})\text{O}_2$, and $\text{Gd}(\text{Dy})_2\text{O}_3$, respectively, alloyed with SiO_2 and Al_2O_3 , have been proposed as alternative high-k gate dielectrics for these advanced Si devices with decreased dimensions and increased levels of integration [7]. Increases in k relative to SiO_2 permit the use of physically thicker films to obtain the same effective capacitance as devices with physically thinner SiO_2 gate dielectrics, providing potential for significantly decreased direct tunneling. However, decreases in direct tunneling associated with this increased physical thickness are negated in part by reductions in the conduction band offset energies that define the tunneling barrier between the Si substrate and the dielectric. This paper develops a classification scheme for non-crystalline oxide-based dielectrics [8], and uses this as the basis for molecular orbital, MO, calculations that have established an inherent correlation between the energy difference of transition metal atomic $n+1$ s- and n d-states and the conduction band offset energies between transition metal oxides and oxide alloys and Si [9,10]. These offset energies determine i) the barrier for direct tunneling between the Si substrate and the transition metal dielectric, and ii) the activation energy for

injection into localized transition metal anti-bonding states in the silicate and aluminate alloys. The paper then extends the new insights obtained for this new understanding of the fundamental electronic of transition metal and rare earth oxide non-crystalline alloys to transition metal chalcogenide non-crystalline alloys. For example, it establishes a theoretical approach for electronic structure of amorphous semiconductors in which the coordination of the constituent atoms is outside the confines of the 8-N rule description that applies to amorphous Se, and $\text{As}_2\text{S}(\text{Se})_3$, $\text{GeS}(\text{Se})_2$, etc [6].

As applied to the transition metal and rare earth oxides and their alloys, the empirical model of Ref. 10 has shown that the lowest lying conduction bands in crystalline transition metal elemental and binary oxides are derived from atomic d-states of the transition metals. The *ab initio* MO model of this paper demonstrates this assignment is not restricted to elemental and binary crystalline oxides, but applies more generally to non-crystalline transition metal oxides and their alloys as well [11-13]. This approach and the qualitative electronic structure results are directly transferable to transition metal chalcogenides in which sulfur or selenium atoms replace oxygen, and the p-state derived valence bands of S and Se do not overlap the d-state derived conduction bands of the transition metal atoms. However, there are qualitatively different electronic and optical properties in transition metal telluride alloys that result from the overlap of Te 5p valence bands with anti-bonding transition metal d-states.

2. Classification of non-crystalline oxides

Zallen [14] has identified and discussed three different atomic scale amorphous morphologies for non-crystalline solids i) continuous random networks, crn's, as exemplified by SiO_2 with predominantly covalent bonding between the constituent atoms, ii) modified continuous random networks, mcrn's, as exemplified by silicate alloys in which metal atom ionic bonds *disrupt* and *modify* the covalently bonded crn structure, and iii) random close packed, rcp, non-periodic solids comprised entirely of negative and positive ions. A classification scheme based on bond ionicity is used to distinguish three different groups of non-crystalline dielectrics with these three distinct amorphous morphologies [8].

There are several different ways to define bond ionicity. The most rigorous way is through calculations of the electronic structure with the application of an *atomic scale metric* such as an atomic radius that is defined in a self-consistent manner and preserves overall charge neutrality. However, there is an intimate relationship between electronegativity [15], X , and the fundamental atomic electronic structure that is reflected in the variation of X across the periodic table. This means that X provides an appropriate metric for defining a bond ionicity that is correlated directly with the electronic structure of the constituent atoms. A definition of bond ionicity, I_b , as originally introduced by Pauling, is the basis for a classification scheme of this paper [15].

For example, if $X(\text{O})$ is the Pauling electronegativity of oxygen, 3.44, and $X(\text{Si})$ is the corresponding electronegativity of silicon, 1.90, then the electronegativity difference between these two atoms, $\Delta X = X(\text{O}) - X(\text{Si})$, is 1.54. Applying Pauling's empirical definition of bond ionicity, I_b ,

$$I_b = 1 - \exp(-0.25(\Delta X)^2), \quad (1)$$

gives a value of I_b for Si-O bonds of $\sim 45\%$. The range of ΔX values for the oxides of interest in this paper ranges from about from 1.5 to 2.4. For this range of ΔX , I_b is approximately a linear function of ΔX , so that ΔX and I_b are functionally *equivalent* scaling variables. It is important to understand that charge localization on the silicon and oxygen atoms, i.e., effective ionic charges, cannot be determined directly from these values of bond ionicity. In SiO_2 , there are π -bonding interactions between silicon atom states with d-like symmetries that are the acceptor states for a back donation of charge from oxygen 2p π states that make the definition of an effective ionic charge a more subtle, and inherently complex issue [16,17].

The non-crystalline oxides, and As and Ge chalcogenides as well, with ΔX up to about 1.5 form covalently-bonded continuous random networks, crn's, in which the constituent atoms have a coordination that reflects its primary chemical valence; e.g., two for O, S and Se, three for N and As, and four for Si and Ge [14]. The bonding in these crn materials obeys the 8-N rule independent of any π -bonding contributions that arise from back donation into d-like polarization states of the P, As, Si or Ge atoms [4]. The glass forming character of these materials, as well as their low defect densities in thin films and bulk glasses, is correlated with the number of bonding constraints per atom and has been discussed in detail in a series of seminal papers by Phillips and his coworkers [18-21].

The second class of non-crystalline dielectrics form modified crn's, mcrn's, which include

ionic bonding arrangements of metal atoms that *modify and disrupt* the network structure. This class of dielectrics is characterized by values of ΔX between about 1.6 and 2.0, or equivalently bond ionicities between about 47 and 67%. The most extensively studied and characterized oxides in this group in are the metal atom silicate alloys, for example SiO_2 that has been alloyed with Na_2O , CaO , TiO_2 , ZrO_2 , etc., and quenched from the melt [14]. This class also includes deposited thin film Al_2O_3 , TiO_2 and Ta_2O_5 , and transition metal atom silicate alloys such as $(\text{Zr}(\text{HfO}_2)_x(\text{SiO}_2)_{1-x})$ in the composition range up to about $x \sim 0.5$ [8]. The non-crystalline range of alloy formation in deposited thin films is increased significantly with respect to what it is in bulk glasses quenched from the melt. The coordination of oxygen atoms in crn's is typically two, and increases to approximately three in the mcrn's (see Table 1). As examples, the average coordination of oxygen is 2.8 in thin film Ta_2O_5 and 3.0 in Al_2O_3 , and increases from 2 to 3 in the group IVB silicate alloys as the ZrO_2 or HfO_2 fraction, x , is increased from doping levels less 0.01 up to alloy levels of 0.5.

Table 1. Electronegativity difference, ΔX , average bond ionicity, I_b , and metal and oxygen coordination for SiO_2 and high-k alternative dielectrics. The $(\text{La}_2\text{O}_3)_2(\text{SiO}_2)_1$ alloy contains both O ions and silicate groups, and as such the O atoms have more local coordinations of 4 and 3, respectively.

DIELECTRIC	ΔX	I_b	COORDINATION M, M or Si	COORDINATION O
CONTINUOUS RANDOM NETWORKS			metal / silicon	oxygen
SiO_2	1.54	0.45	4	2.0
CRN'S WITH NETWORK MODIFIERS				
Al_2O_3	1.84	0.57	4 and 6 (3:1)	3.0
Ta_2O_5	1.94	0.61	6 and 8 (1:1)	2.8
TiO_2	1.90	0.59	6	3.0
$(\text{ZrO}_2)_{0.1}(\text{SiO}_2)_{0.9}$	1.61	0.48	8 and 4	2.2
$(\text{ZrO}_2)_{0.23}(\text{SiO}_2)_{0.77}$	1.70	0.51	8 and 4	2.46
$(\text{ZrO}_2)_{0.5}(\text{SiO}_2)_{0.5}$	1.88	0.59	8 and 4	3.0
$(\text{TiO}_2)_{0.5}(\text{SiO}_2)_{0.5}$	1.72	0.52	6 and 4	2.5
$(\text{Y}_2\text{O}_3)_1(\text{SiO}_2)_2$	1.88	0.59	6 and 4	2.86
$(\text{Y}_2\text{O}_3)_2(\text{SiO}_2)_3$	1.93	0.61	6 and 4	3.0
$(\text{Y}_2\text{O}_3)_1(\text{SiO}_2)_1$	1.99	0.63	6 and 4	3.11
$(\text{Al}_2\text{O}_3)_4(\text{ZrO}_2)_1$	2.02	0.64	4 and 8	3.0
$(\text{Al}_2\text{O}_3)_3(\text{Y}_2\text{O}_3)_1$	1.97	0.62	4 and 6	3.0
RANDOM CLOSE PACKED IONS				
HfO_2	2.14	0.68	8	4.0
ZrO_2	2.22	0.71	8	4.0
$(\text{La}_2\text{O}_3)_2(\text{SiO}_2)_1$	2.18	0.70	6 and 4	3.5
Y_2O_3	2.22	0.71	6	4.0
La_2O_3	2.34	0.75	6	4.0

The third group of non-crystalline oxides has a random close packed ionic amorphous morphology [14]. This class of oxides is correlated with $\Delta X > 2$, and a Pauling bond ionicity of greater than ~67%. This group includes transition metal oxides that are deposited by low temperature techniques including plasma deposition, and sputtering with post-deposition oxidation [7]. The coordination of the oxygen atoms in these rcn structures is typically four.

Table 1 includes i) a list of representative elemental and binary oxide alloys, as well as values of ii) ΔX , iii) I_b , and iii) the average O-atom and cation bonding coordinations. In summary, values of ΔX of ~1.6 and ~2.0 separate these elemental and binary into three different groups: i) crns for ΔX up to 1.6, ii) mcrn's for ΔX between ~1.6 and 2.0, and iii) rcn ionic structures for $\Delta X > 2$. As

The average coordination of O-atoms is 2 for the crn's, between 2 and 3 for the mcrn's and greater than 3, and typically four for the rcn oxides. The values of I_b , calculated from Eqn. [2], that separate these three groups, are approximately 47% and 67%.

Fig. 1 contains a plot of the average oxygen atom coordination as a function of the average bond ionicity, I_b . The values of oxygen atom coordination are either i) inferred from measurements or measured directly [22], or ii) determined from crystalline compounds [16]. Since I_b is a linear function of ΔX for the oxides, and silicate and aluminate alloys of interest, the average oxygen atom coordination also scales linearly with ΔX . The approximately linear variation suggests a fundamental relationship between charge localization of the oxygen atom and bonding coordination. A classification scheme for chalcogenides can be formulated in terms of electronegativity; however, the scale is severely compressed due to the decreased electronegativities of S, Se and Te with respect to O. However, a classification scheme based on the bonding coordination of the chalcogen atoms is more useful. For example, it separates chalcogenides into groups with inherently different amorphous morphologies, the most important of which are crn's and mcrn's.

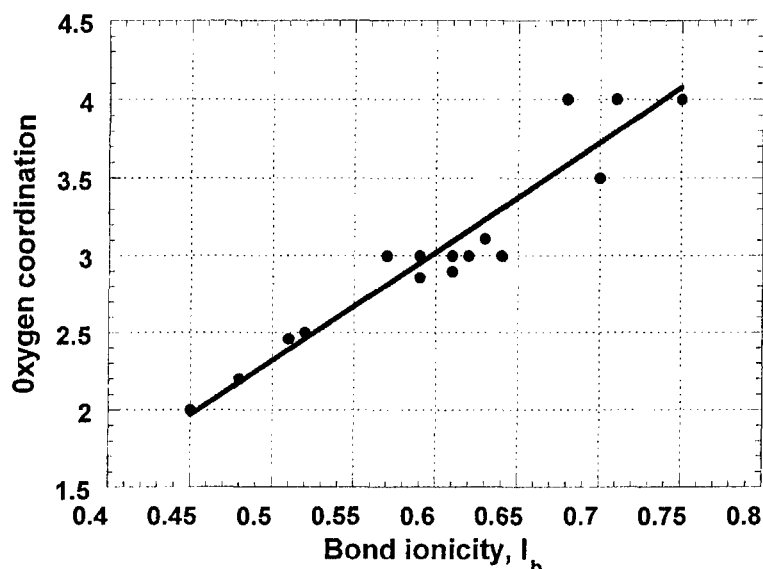


Fig. 1. Average oxygen atom coordination as a function of the average bond ionicity, I_b for SiO_2 and elemental and binary oxides that have been considered as alternative high- k gate dielectrics.

Returning to the oxides, the emphasis of the next few sections of the paper will be on transition metal silicate and aluminate, pseudo-binary alloys of group IIIB and IVB transition metals and rare earth lanthanides, with either SiO_2 or Al_2O_3 , respectively. These pseudo-binary alloys have modified continuous random network structures in which the transition metals atoms either disrupt the work crn structure of SiO_2 , or substitute for the six-fold coordinated Al^{3+} ions of the non-crystalline Al_2O_3 structure [22]. The coordination of group IVB transition metals such as Zr and Hf has been shown to be a function of the $\text{Zr}(\text{Hf})\text{O}_2$ fraction in the low concentration silicate alloys [23], so that both tetrahedral and higher coordinations up to eight oxygen neighbors must be addressed. In order to evaluate the potential of these alloys for applications as high- k gate dielectrics for advanced semiconductor devices, it is necessary to understand their electronic structure. Conversely, a quantitative understanding of electronic structure, particularly the atomic parentage of the valence band states, and the lowest conduction band or anti-bonding states provides a basis for interpretation of many important optical and electrical experimental results.

3. Molecular orbital calculations

Fig. 2 is a molecular orbital energy level diagram for a group IV transition metal, e.g., Ti, in an octahedral bonding arrangement with six oxygen neighbors [11-13]. Each oxygen atom is assumed to provide one σ and two π 2p-electrons for potential bonding with the neutral group IV atoms, each of which contributes four additional electrons. The symmetries and π or σ character of the resulting orbitals are determined by symmetries of the group IVB and oxygen atomic states. Of the twenty-two available electrons, fourteen are involved σ and π bonding, and the remaining four are in oxygen atom

non-bonding orbitals with π character. The calculations show that the spatial localization of the transition metal atomic d-states gives a solid state broadening significantly less than their energy separation relative to transition metal s-states. The top of the valence band is associated with non-bonding π orbitals of oxygen atom p-states, and the first two conduction bands are associated with transition metal d-states. In order of increasing energy these conduction bands have the following symmetries $t_{2g}(\pi^*)$, and $e_g(\sigma^*)$. The next conduction band is derived from transition metal s-states with $a_{1g}(\sigma^*)$ character. The energy separation between the top of the valence band and the $a_{1g}(\sigma^*)$ band edge defines an effective *ionic band gap* with essentially the same energy as that of non-transition metal insulating oxide; i.e., $\sim 8-9$ eV [13]. Higher lying conduction bands are derived from transition metal p-states with both σ and π character, $t_{1u}(\sigma^*, \pi^*)$. The ordering of the first three conduction bands in crystalline TiO_2 has been verified by electron energy loss and X-ray spectroscopies, which confirm the relative sharpness of the $t_{2g}(\pi^*)$, and $e_g(\sigma^*)$ bands, the increased width of the $a_{1g}(\sigma^*)$ band, as well as an ionic band energy > 8 eV [24].

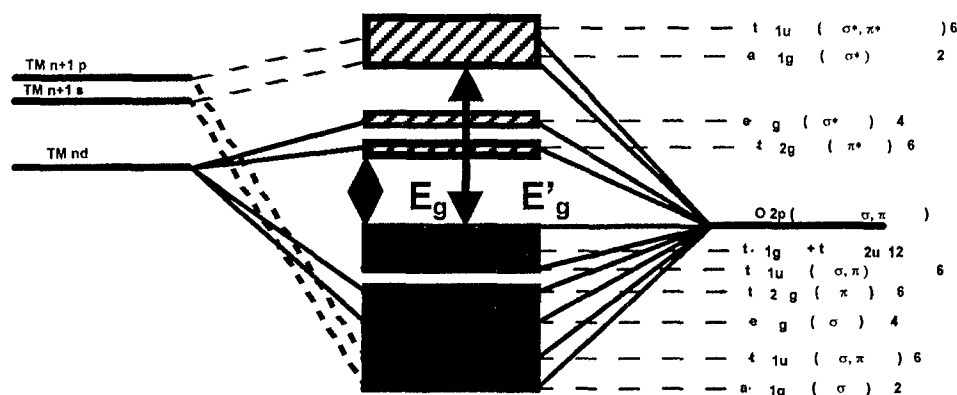


Fig. 2. Relative orbital energies for a group IVB transition metal in an octahedral bonding geometry with six oxygen atom neighbors.

A group theoretical analyses of the relative energies and symmetries of valence and conduction band orbitals for four- and six-fold coordinated transition metal atoms in tetrahedral and octahedral bonding environments [13,16] reveals a different ordering and σ and π assignment of the transition metal d-states (see Table 2). The lowest lying anti-bonding or conduction band states are derived from the triply degenerate transition metal d-states for the octahedral bonding, and the doubly degenerate d-states for the tetrahedral bonding. The symmetry of these anti-bonding states can be correlated directly with the spatial orientation between the d-orbitals and the oxygen neighbors. If the orbitals of one of the d-states groups, t_g or e_g , can be directed toward the nearest neighbors, then these orbitals are involved in σ bonding interactions, whilst the other set is involved in π bonds. This establishes the ordering in relative energy of the bonding and anti-bonding derived from these d-states. This type of analysis can be readily extended to other coordinations; e.g., eight-fold, and other bonding symmetries, e.g., cubic and trigonal prism. The reader is referred to Refs 13 and 16 for details, including the group theory symmetry designations of the bonding, non-bonding and anti-bonding states.

Table 2. Comparison of bonding, non-bonding and anti-bonding states for octahedral and tetrahedral coordination of transition metal atoms.

Symmetry Designation*	Octahedral Coordination	Tetrahedral Coordination
Bonding States, (b)	$a_{1g}(\sigma^b)$ [2], $t_{1u}(\sigma^b, \pi^b)$ [6], $e_g(\sigma^b)$ [4], $t_{2g}(\pi^b)$ [6]	$a_1(\sigma^b)$ [2], $t_2(\sigma^b, \pi^b)$ [6], $e(\pi^b)$ [4], $t_1(\pi^b)$ [6]
Non-bonding States (1 σ and 2 π electrons/O)	$t_{1u}(\sigma, \pi)$ [6], $t_{1g} + t_{2u}$ [12]	$t_1(\pi)$ [12]
Anti-bonding States, (*)	$t_{2g}(\pi^*)$ [6], $e_g(\sigma^*)$ [4], $a_{1g}(\sigma^*)$ [2], $t_{1u}(\sigma^*, \pi^*)$ [6]	$e(\pi^*)$ [4], $t_2(\sigma^*, \pi^*)$ [12], $a_1(\sigma^*)$ [2], $t_2(\sigma^b)$ [6]

* The numbers in brackets are the number so states available in each orbital. The occupancy depends on the number of electrons available from the transition metal (i.e., its formal ionization state), and coordination of the oxygen atom ligands.

The calculations further demonstrate that the energy difference between the lowest conduction band with $t_{2g}(\pi^*)$ symmetry, and the bottom of the $a_{1g}(\sigma^*)$ band scales with the difference in energy between the $n+1$ s- and n d-states of the transition metal atoms [25]. The argument for this proceeds as follows: since the ionic band gaps, defined in terms of transitions between the p-derived valence band states of the oxygen and the s-derived conduction band states of the transition metals, are at about the same energy, ~ 8 -9 eV, the larger the energy difference between the transition metal atomic s- and d-states, and the closer the d-state bands are to the top of valence band. This means that the smallest band gaps of transition metal oxides and silicate and aluminate alloys will scale approximately with the difference in energy between the transition metal s- and d-states. Since the transition metal s-states are all at approximately the same energy with respect to vacuum, this means additionally that the lowest band-gaps are expected to scale with the energy difference between oxygen or chalcogen atom p-states and the transition metal d-states (see Fig. 3).

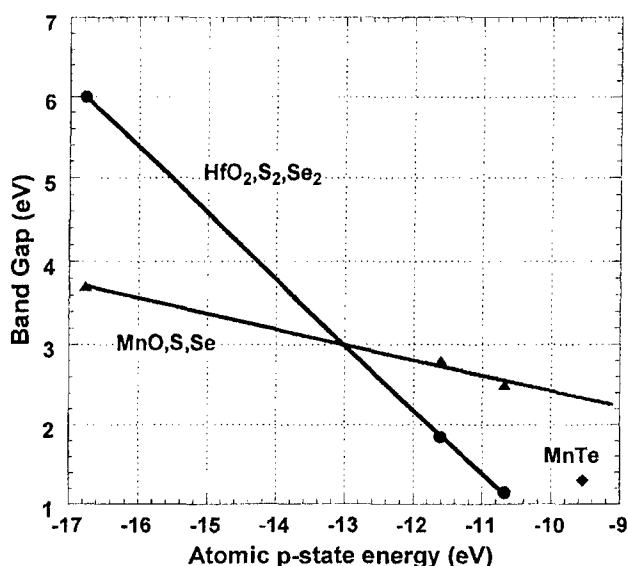


Fig. 3. Optical band gap versus the energy of the atomic p-states of oxygen, sulfur and selenium for i) HfO_2 , HfS_2 and HfSe_2 , and ii) MnO , MnS , and MnSe .

The scaling in Figs. 3 and the results in Table 3 show that energy level schemes similar to Fig. 2 apply to transition metal chalcogenides in which oxygen is replaced by sulfur and selenium [19,20]. Fig. 3 is a plot i) optical band gap versus the energy of the atomic p-states of oxygen, sulfur and selenium for (a) HfO_2 , HfS_2 and HfSe_2 [4,19], and (b) MnO , MnS , and MnSe [20], and Table 3 compares the optical band gap versus atomic n d-state energy of the transition metal atom for group IVB oxides, sulfides and selenides [4,19]. The plot in Fig. 3 shows that for a given transition metal, the band gap scales with the p-state energy of the chalcogen, whereas the results in Table 3 show that for a fixed negative ion, O or S, the band gap scales with the energy of the transition metal atom d-state. The results in Table 3 show that for a given cation, O, S or Se, the optical band gap scales as the energy of the atomic d-state of the transition metal.

Table 3. Comparison between band gaps of group IV B oxides, sulfides, and selenides, and d-state energy of group IVB transition metals, Ti, Zr and Hf.

group IVB atom	d-state (eV)	band gap (eV)		
		oxide	sulfide	selenide
Ti	-11.1	3.05 6.0	<0.5	<0.5
Zr	-8.5	6.0	1.9	1.1
Hf	-8.8	6.0	1.9	1.15

4. Band offset energy

The band offset energy between the conduction band of Si and the empty anti-bonding or conduction band states of a high- k dielectric is important in metal-oxide-semiconductor, MOS, device performance. It defines the barrier for direct tunneling, and/or thermal emission of electrons from an n^+ Si substrate into the dielectric. In alloys such as Al_2O_3 - Ta_2O_5 , or SiO_2 - ZrO_2 , it defines the energy of localized Ta and Zr transition metal electron trapping states, respectively, relative to the Si conduction band minimum [28].

The energies with respect to vacuum of the atomic $n+1$ s-states of the group IIIB, IVB and VB are approximately constant, ~ -7 eV. The band gaps of the transition metal oxides have been shown in Table 3 to scale with the energies of the n d-atomic states of the transition metal atoms. Based on the molecular orbital model of Fig. 2, it is reasonable to assume that the difference in energy between the lowest anti-bonding d-states and s-states scales with the difference in the energies of the atomic $n+1$ s- and n d-states. If this is the case, then the band offset energy between the conduction band of Si and the lowest conduction band of the transition metal oxides must also scale with the absolute value of the difference between the energies of the atomic $n+1$ s- and n d-states (see Fig. 2). Fig. 4 displays the band offset energies of transition metal oxides from Refs. 9 and 10 as a function of the atomic s- state to d-state energy difference. The data points in Fig. 4 display an approximately linear dependence, supporting the assumptions made on the basis of the molecular orbital model description of the electronic structure of the transition metal oxide derived conduction band states.

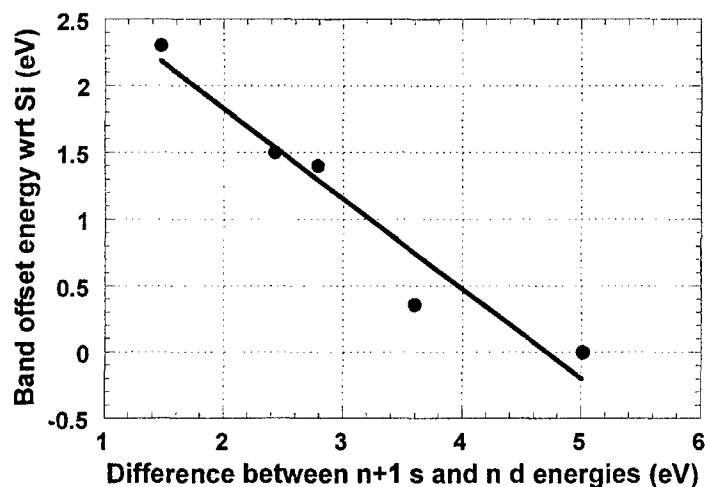


Fig. 4. Band offset energies from versus the absolute value of the $n+1$ s - n d energy difference for transition metal elemental oxides and silicates.

5. Recent experimental results

5.1. Trapping at Transition Metal Sites in Al_2O_3 - Ta_2O_5 Alloys

Alloys of Al_2O_3 and Ta_2O_5 with different concentrations of Ta_2O_5 have been prepared by remote plasma assisted deposition onto hydrogen terminated Si(100) substrates and incorporated into MOS capacitors. These alloys are pseudo-binary in character with Ta-O and Al-O bonds, but no spectroscopic evidence for Al-Ta bonds; the details are discussed in Ref. 21. In addition as shown in Ref. 9, there is a large anisotropy between the conduction and valence band offset energies of Ta_2O_5 , ~ 0.3 eV and 3.0 eV, whilst the corresponding offset energies for Al_2O_3 show a smaller anisotropy, 2.1 eV as compared with 3.7 eV. Fig. 5 indicates the leakage current from an n^+ Si substrate as a function of temperature. Flat band voltage shifts, and hysteresis in for capacitance-voltage C-V, data in the low temperature regime, are consistent with electron trapping, whereas the C-V data in the high temperature regime are consistent with emission out of trapping states. Combining these C-V data with the energy band scheme of Fig. 2, the activation energy in the low temperature regime, ~ 0.3 eV, for electron trapping is assigned to the difference in energy between the Si conduction band and the lowest lying $t_{2g}(\pi^*)$ state of a six fold coordinated Ta atom, and the activation energy at higher temperatures, ~ 1.5 eV, is assigned to emission out of these Ta traps into the conduction band of the Al_2O_3 matrix. These two energies are consistent with the measured band offset energy of Ta_2O_5 with

respect to Si, ~ 0.36 eV, as determined from X-ray photoelectron spectroscopy, XPS [9], and the energy difference between the measured band offset energies for Al_2O_3 and Ta_2O_5 with respect to Si, ~ 1.7 eV, also measured by XPS.

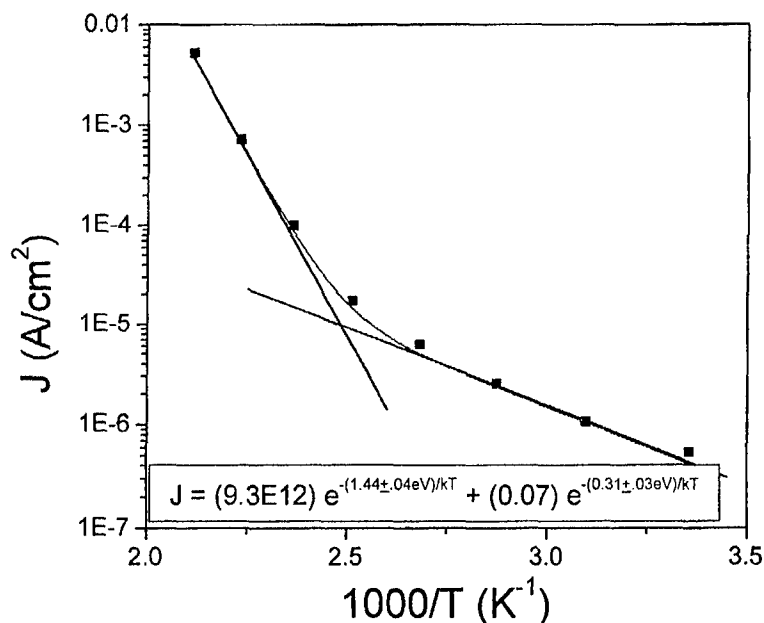


Fig. 5. Current versus $1/T$ for a capacitor with a Ta_2O_5 - Al_2O_3 alloy dielectric, $x \sim 0.4$.

5.2. Coordination dependent dynamic infrared effective charges

A comparative study of the infrared reflectivity of group IVB and VIB crystalline dichalcogenides, $\text{Zr}(\text{Hf})\text{S}(\text{Se})_2$ and $\text{Mo}(\text{W})\text{S}(\text{Se})_2$, respectively, has yielded significantly different dynamic transverse infrared, ir , effective charges, e^*_T , for vibrational modes with atomic displacements perpendicular to the crystalline c -axis (for details see Ref. 29). The group IVB transition metals are in an octahedral bonding geometry, whilst the group VIB transition metals are in trigonal prism geometry. The values of e^*_T , for the group IVB dichalcogenides are about 8 to 9 times larger than for the group VIB dichalcogenides. e^*_T is typically ~ 4 - $5e$ for the group IV chalcogenides, and $\sim 0.25e$ for the group VI chalcogenides. These differences in e^*_T can not be explained on the basis of an ionic bonding model; e.g., the bond ionicity for Zr-S is ~ 0.3 , so that the ionic charge would be no more than about $1.2e$. However, in the context of the MO model, the charges are dynamic character, and the large difference derives an increased dynamic contribution due to the more symmetric bonding orbital geometry at the octahedral bonding sites of the group IVB chalcogenides.

A similar effect has been identified for the Zr and Hf silicates, where there is a significant enhancement of the dielectric constant for low concentration silicate alloys [23]. In this instance, the increase has been correlated with a change in bonding coordination. In the low concentration regime, analysis of extended X-ray absorption fine structure spectra, EXAFS, has indicated a Zr atom coordination of about four, whilst for the stoichiometric silicates, e.g., ZrSiO_4 , the coordination is eight. The bonding geometry at the four-fold site is presumed to be tetrahedral, whereas, at the higher concentrations it is assumed to be the same as in the crystalline zircon phase, i.e., a cubic prism [30]. An empirical model indicates a decrease in e^*_T by at least a factor of two between these two geometries, with the effective charge being larger in the more symmetric tetrahedral geometry. A linear combination of the transition metal e_g d-states can be directed along the tetrahedral directions when there is mixing with the transition metal s-states. These four orbitals are equivalent in character, hence the high symmetry of this coordination. However, expansion to eight fold coordination does not provide eight equivalent orbitals, hence a distortion from a perfect cubic bonding arrangement, a reduction in symmetry, and a decreased dynamic effective charge. This is underlying region for the bond order reduction of two between the four and eight fold bonding coordinations of Ref. 23.

5.3. Localized anti-bonding d-state derived levels in Zr silicate alloys

Fig. 6 displays X-ray absorption spectroscopy, XAS, spectra for series of Zr silicate alloys, $(\text{ZrO}_2)_x(\text{SiO}_2)_{1-x}$, $x \sim 0.05, 0.2, 0.5$ and 1.0 as obtained at Brookhaven National Laboratory; details of these measurements [31] and the alloy preparation are described elsewhere as well. The spectral features are assigned to dipole-allowed transitions between $M_{2,3}$ p-core states of the Zr atoms, and conduction band states derived from the 4d (a and b, and a' and b') and 5s (c and c') atomic states of Zr. The bonding arrangements of Zr and Si atoms in these alloys have been addressed in Refs. 22 and 23. As-deposited alloys prepared by plasma deposition are non-crystalline and pseudo-binary with Si-O and Zr-O bonds, but no detectable Zr-Si bonds. After annealing at 900 to 1000°C the $x = 0.5$ alloys phase separates in SiO_2 and crystalline ZrO_2 , and $x = 1.0$ is also crystallizes. The energies of the highlighted features in the $M_{2,3}$ XAS spectra in Fig. 6 are independent, up to an experimental uncertainty of ± 0.1 eV, of the alloy composition and state of crystallinity. The independence of these spectral features on alloy composition, and the relatively small changes that take place on crystallization of a ZrO_2 phase after annealing are consistent with a molecular orbital description. The MO calculations indicate localization of d-states on the TM atoms with energies determined predominantly by coordination and symmetry of their oxygen neighbors, and are not influenced by either their second neighbors or the absence or presence of long range order.

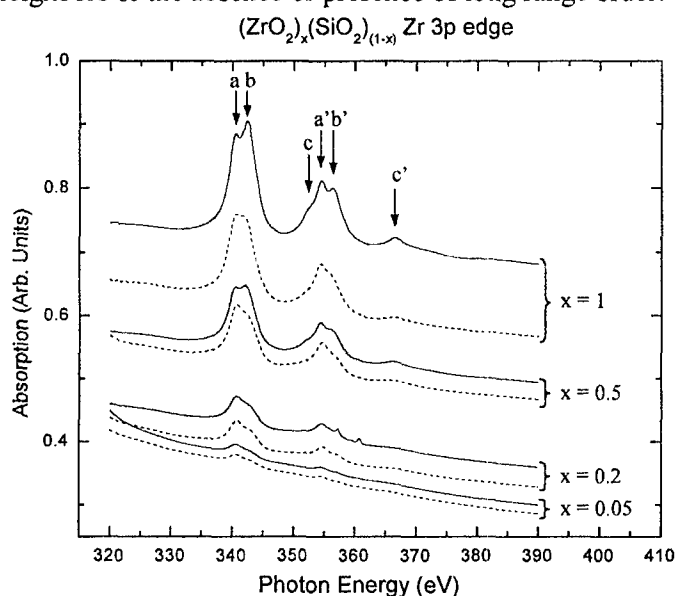


Fig. 6. X-ray absorption spectra as a function of photon energy for excitation from Zr $M_{2,3}$ p-states in empty Zr 4d and 5s states of Zr silicate alloys. Before and after a rapid thermal anneal at 1000 C. The letters a, b and c and a', b' and c' designate the energy differences between the M_2 and M_3 p-states, respectively, and the anti-bonding Zr states.

6. Non-crystalline chalcogenides

Calculations based on the Pauling bond-ionicity approach have also been applied to amorphous morphology and properties of transition metal chalcogenide alloys, e.g., Ni in As_2Se_3 based alloys. Since the electronegativities of S and Se are significantly smaller than that of oxygen, scaling based on bond ionicity is compressed, and neither X nor I_b is an appropriate scaling variable. On the other hand bond coordination is more significant, in particular the breakdown of the 8-N rule in which chalcogen atoms are assumed to have a coordination of two. As indicated in Fig. 1 and Table 1, the 8-N rule breaks down whenever SiO_2 is alloyed with a transition metal oxide. A similar situation prevails for alloys of chalcogen compounds such as As_2Se_3 , and transition metal chalcogenides that are alloys of As_2Se_3 and Cu_2Se or NiSe . For example, the bonding coordination of Se increases from two to four in the alloy system: $\text{As}_2\text{Se}_3\text{-Cu}_2\text{Se}$, and this increase in Se coordination also occurs in disordered alloys with compositions along the pseudo-binary join line from As_2Se_3 to CuAsSe_2 [32]. In addition, the energies of the transition metal electronic states relative to the conduction and valence bands of a chalcogenide alloy host, the occupancy of these states and the

transition metal concentration are the important factors in promoting a transition from insulating to metallic conductivity as a function of increasing metal atom content.

This section of the paper addresses two different types of chalcogenide materials that do not conform to the 8-N rule [4], alloys containing: i) tellurium, such as the Te, As, Ge glass used by the IBM group for laser writing [33] the memory materials initially studied by ECD, Ge, Te, Sb or As and S alloys [1,34], and ii) transition metals such as Ni [35-37]. Consider first the changes in bonding and structure that take place when Te is substituted for either S or Se in chalcogenide compounds and alloys.

Building on the comparisons made between transition metal oxides, sulfides, and selenides earlier in this paper there are two issues to consider that are different for the corresponding tellurides; i) band overlap between the valence band states of Te and the d-states of the transition metals, and ii) changes in crystalline structure associated with the Te substitutions. Consider first MnO and the Mn chalcogenides. The results presented in Fig. 3 and in Ref. 27, indicate: i) scaling between optical band gaps for the oxide, sulfide and selenide, and the atomic energy of the valence band p-state of the anion, and ii) a breakdown of this scaling relationship for MnTe as indicated by the point for MnTe that is below the linear fit. The discussion in Ref. 27 has attributed the departure from linear scaling to a qualitatively and quantitatively different electronic structure of MnTe in which the d-states of Mn overlap the p-states of Te. This overlap also promotes a change in the crystal structure from rock salt, NaCl, to the nickel arsenide, NiAs. In this example MnTe is still a semiconductor, whereas in the transition metal dichalcogenides that involve a smaller number of d-electrons, a similar overlap of anti-bonding d-bands of the transition metal with the p-states of Te that comprise the valence band, results in metallic behavior [26]. The Te doped alloys used in optical and electronic switching [1,34] generally have significantly reduced band gaps with respect to their Se and S analogs, and in addition display transitions to metallic conductivity with, and without crystallization.

Differences in the properties between Te containing non-crystalline chalcogenides and those containing S and Se are also correlated with increased coordination of the Te atoms [35]; i.e., a breakdown of the 8-N rule. This increase in coordination requires the use of d-orbitals of the Te changing the basic electronic structure and the resulting properties. The large differences in the band gap and optic mode vibrational frequencies between crystalline and amorphous Te are consistent with these changes in the effective coordination and the resulting valence band structure [38].

The second example of a transition metal induced change in conducting properties occurs in chalcogenides that have been alloyed with Ni. Two different effects have been reported: i) crystallization resulting in metallic conductivity [37], and ii) metallic conductivity in the non-crystalline state that occurs above a threshold concentration of Ni [35,36]. The second of these effects is attributed to local bonding arrangements comprised of i) Ni with six Se neighbors, and ii) an increase in the coordination of Se as well. This arrangement has an odd number of electrons available for bonding resulting in a partially filled valence band and the potential for metallic conductivity. Based on the atomic 3d-state energy of Ni and the valence p-state energy of Te, the Ni d-band overlaps the Te valence states, so that at a sufficiently high concentration of Ni, electrons can be transported between localized Ni bonding sites resulting in the observed metallic conductivity.

7. Discussion

This paper has presented a classification scheme for high-k dielectrics that separates SiO₂ and the alternative non-crystalline dielectrics into three groups with qualitatively different amorphous bonding morphologies. This paper has emphasized group IIIB and IVB silicate and aluminate alloys that have a modified continuous random network structure. In the silicate alloys, the transition metal atoms disrupt the covalent bonding of the host SiO₂ network with the transition metal atoms displaying a higher bond ionicity with respect to their oxygen neighbors. The classification scheme is integrated into a molecular orbital model that is used to establish energy level diagrams for insulating transition metal oxides and their silicate and aluminate alloys. The ordering of the conduction band or anti-bonding states is determined by the symmetry and coordination at the transition metal atom, and their energy level separations are correlated with differences between σ and π overlap integrals [11-13]. One test of the model is the scaling of the optical band gap with anion atomic p-state energy for a given transition metal; e.g., HfO₂, HfS₂ and HfSe₂. The results in Fig. 3 show that as the anion becomes less electronegative from oxygen, to sulfur and selenium, the band gap between the lowest lying transition metal d-states and valence band derived from anion p-states, decreases in direct

proportion to changes in the anion atomic p-state energies. This establishes that the transition metals d-states are not significantly shifted in energy with respect to changes in the anion electronegativity. In a complementary manner, the data in Table 3 establish that the energy difference between the valence band derived from chalcogen or oxygen atom p-states, and the first conduction associated with $t_{2g}(\pi^*)$ d-states scales with the atomic d-state energy of the transition metal. The results in Fig. 4 show that conduction band offset energies with respect to Si display a linear scaling in which the energy of the bottom of the lowest conduction band is correlated with the energy difference between the transition metal $n+1$ s- and n d-atomic states. The results displayed in Fig. 5 indicate that the energies of transition metal d-states associated with the lowest unoccupied orbitals have approximately the same energy relative to the Si conduction in an elemental oxide, Ta_2O_5 , that they do in a binary alloy, Al_2O_3 - Ta_2O_5 . The results in Fig. 6 indicate the energies of the Zr d-states that define the lowest conduction bands are independent of the ZrO_2 concentration in Zr silicate alloys, and independent of crystallization as well. The results presented above support the validity of the local molecular orbital description of the electronic structure of transition metal oxides and their silicate and aluminate alloys. The model is being refined to include additional solid state effects associated with renormalization of orbitals and orbital energies that includes interactions with more distant neighbors. Based on the results in Figs. 5 and 6, these interaction are not expected to significantly shift the average energies of anti-bonding states derived from transition metal atomic d-states, but are expected to yield a measure of their width which can be studied experimentally with X-ray absorption and electron energy loss spectroscopies.

The results displayed in Fig. 4 are of particular importance to advanced Si devices. First, they demonstrate that the band offset energies that define the tunneling barrier, scale with atomic properties, i.e., the energy separation between $n+1$ s and n d states of transition metal and rare earth atoms. Second, they demonstrate that the energies of intrinsic localized states present in transition metal alloys also scale with the energy difference between the Si conduction band and the transition metal d-state energy. Finally, they provide an important atomic scale metric for identification of potential high-k gate dielectrics. The larger the energy separation between the energies of the $n+1$ s- and n d-states of transition metal atoms of an elemental oxide, or transitional metal silicate or aluminate alloy, the higher the conduction band offset energy between Si and that dielectric, and the lower the direct tunneling and/or interfacial and bulk electron trapping. The model raises additional issues with respect to tunneling in transition metal silicate and aluminate alloys. For alloys that are transition metal oxide rich, the effective barrier for tunneling will be determined primarily by the lowest anti-bonding or conduction band states derived from the transition metal d-states, either the $t_{2g}(\pi^*)$ or $e_g(\sigma^*)$ band depending on the coordination of the particular transition metal. However, localized transition metal derived $t_{2g}(\pi^*)$ or $e_g(\sigma^*)$ states in SiO_2 or Al_2O_3 rich alloys will act more like traps than conduction band states, and their effect on tunnel transport is yet to be determined. For example, they clearly provide a pathway for increased tunneling, but will not necessarily define an effective barrier for direct tunneling.

There are other factors that contribute to the performance of advanced Si devices. Paramount among them are interfacial defects that can trap electrons and/or holes, and/or be a source of fixed charge that shifts threshold voltages and reduces channel mobilities in field effect transistors. This paper has addressed one class of interface trapping states that are present in silicate and aluminate alloys. It has not addressed fixed charge in the interfacial bonding region that is associated with the increased ionic bonding character of alternative transition metal high-k dielectrics, and for a discussion of these effects the reader is referred to Ref. 39.

The structural model for transition metal alloys that has emerged from the classification scheme, combined with the molecular orbital calculations provide insights into contributions to the transverse dynamic infrared effective charge. Contributions of vibrational modes scale as the square of these charges, so that changes in atomic coordination with concentration, or between different transition or rare earth metals, can change their effective charges, and therefore their dielectric constants as well. The two-fold bonding coordination of S and Se in chalcogenide alloys obeying the 8-N rule as in $As_2Se(S)_3$, is increased upon alloying with transition metal selenides in which the coordination of Ni and Se atoms is six. The coordination of Se in As_2Se_3 -NiSe alloys will increase monotonically between two and six as the NiSe concentration is increased. Finally, the properties of non-crystalline chalcogenides containing Te are qualitatively different their S and Se analogs. This is attributed to two factors: i) reduced band gaps due to differences in the energies of the atomic p-states that comprise the valence, and ii) increases in atomic coordination which require d-state participation in the valence band electronic structure.

Acknowledgement

This research is supported by the Office of Naval Research, the Air Force Office of Scientific Research and the SEMATECH/SRC Front End Processing Center.

References

- [1] S. R. Ovshinsky, *Phys. Rev. Lett.* **21**, 1450 (1968).
- [2] S. R. Ovshinsky, *J. Non-Cryst. Solids* **8-10**, 892 (1972); J. Feinleib, S. Iwasa, S. C. Moss, J. P. DeNeuville, S. R. Ovshinsky, *J. Non-Cryst. Solids* **8-10**, 909 (1972).
- [3] D. E. Carlson, C. R. Wronski, *Appl. Phys. Lett.* **28**, 671 (1976).
- [4] N. F. Mott, *AIP Conf. Proc.* **32**, 1 (1976); N. F. Mott, E. A. Davis, *Electronic Processes in Non-Crystalline Solids* (Clarendon Press, Oxford, 1972).
- [5] J. Stuke, *Festkorperprobleme* **IX**, 46 (1969).
- [6] W. Beyer, J. Stuke, *J. Non-Cryst. Solids* **8-10**, 321 (1972).
- [7] G. Wilk, R. W. Wallace, J. M. Anthony, *J. Appl. Physics* (2001), in press.
- [8] G. Lucovsky, *J. Vac. Sci. Technol. A* **19** (2001), in press.
- [9] S. Miyazaki, *J. Vac. Sci. Technol. B* **19** (2001), in press.
- [10] J. Robertson, C. W. Chen, *Appl. Phys. Lett.* **74**, 1164 (1999) and J. Robertson, *J. Vac. Sci. Technol. B* **18**, 1785 (2000).
- [11] H. B. Gray, "Electrons and Chemical Bonding" (W.A. Benjamin, New York, 1962), Chapter. 9.
- [12] C. J. Ballhausen and H. B. Gray, "Molecular Orbital Theory" (W. A. Benjamin, New York, 1964), Chapter. 8.
- [13] P. A. Cox. "Transition Metal Oxides" (Oxford Science Publications, Oxford, 1992), Chapter 2.
- [14] R. Zallen, "The Physics of Amorphous Solids" (John Wiley and Sons, New York, 1983), Chapter 2.
- [15] L. Pauling, "The Nature of the Chemical Bond", Third Edition, (Cornell University Press, Ithaca, NY, 1948), Chapter 2.
- [16] F. A. Cotton, G. Wilkinson, "Inorganic Chemistry, Third Edition", (Interscience, New York, 1972), Chapter 4.
- [17] L. Pauling, *American Mineralogist* **65**, 321 (1960).
- [18] J. C. Phillips, *J. Non-Cryst. Solids* **34**, 153 (1979).
- [19] J. C. Phillips, *J. Non-Cryst. Solids* **43**, 37 (1981).
- [20] G. Lucovsky, J. C. Phillips, *J. Non-Cryst. Solids* **227**, 1221 (1998).
- [21] J. C. Phillips, X. Kerner, *Solid State Commun.* **117**, 47 (2001).
- [22] B. Rayner, H. Niimi, R. Johnson, R. Therrien, G. Lucovsky, F. L. Galeener, in "Proc. of Characterization and Metrology for USLI Technology", *AIP Conf. Proc.* **550**, 149 (2001).
- [23] G. Lucovsky, G. B. Rayner, *Appl. Phys. Lett.* **77**, 2912 (2000).
- [24] L. A. Grunes, R. D. Leapman, C. D. Walker, R. Hoffman, A. B. Kunz, *Phys. Rev. B* **25**, 7157 (1982).
- [25] W. A. Harrison, "Elementary Electronic Structure", (World Scientific, Singapore, 1999).
- [26] J. A. Wilson, A. D. Yoffe, *Advances in Physics*, **18**, 193 (1969).
- [27] J. A. Allen, G. Lucovsky, J. C. Mikkelsen, Jr., *Solid State. Commun.* **24**, 367 (1977).
- [28] R. S. Johnson, G. Lucovsky, J. Hong, *Appl. Surf. Sci.*, these proceedings.
- [29] G. Lucovsky, R. M. White, J. A. Benda, J. F. Revelli, *Phys. Rev. B* **7**, 3859 (1973).
- [30] K. Robinson, G. V. Gibbs, P. H. Ribbe, *The American Mineralogist* **56**, 782 (1971).
- [31] G. Lucovsky, et al. submitted to *Appl. Phys. Lett.* (2001).
- [32] S. H. Hunter, A. Bienenstock, T. M. Hayes, in *Amorphous and Liquid Semiconductors*, ed. by W. E. Spear (University of Edinburgh, 1977), p. 78.
- [33] P. Chaudhari, S. R. Herd, D. Ast, M. H. Brodsky, R. J. Von Gutfield, *J. Non-Cryst. Solids*, **8-10**, 900 (1972).
- [34] F. Betts, A. Bienenstock, C.W. Bates, *J. Non-Cryst. Solids* **8-10**, 364 (1972).
- [35] S. R. Ovshinsky, in Ref. 32, p. 519.
- [36] R. Flasck, M. Izu, K. Sapru, T. Anderson, S. R. Ovshinsky, H. Fritzsche, in Ref. 31, p. 524.
- [37] Y. Sawan, F. Wakim, M. Abu-Zeid, M. El Gabaly, *Proc. 15th Int. Conf. Physics of Semiconductors*, Kyoto, 1980, *J. Phys. Soc. Japan* **49** (Suppl. A), 1163 (1980).
- [38] G. Lucovsky, *Phys. Stat. Sol. (b)* **49**, 633 (1972).
- [39] G. Lucovsky, J. C. Phillips, M. F. Thorpe, in Ref. 22, p. 154.